Scilight

Advanced Antibacterial Materials
https://www.sciltp.com/journals/aam

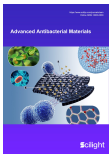

Article

Construction of AIE Molecule-Embedded Long-Persistent Luminescence Coating for Self-Activated Photodynamic Antibacterial Performance

Weizhe Li [1], Li Xiang [1], Sathishkumar Gnanasekar [1,*], Xiaodong He [1], Yunjie Xiang [1], Kun Xu [1], Xi Rao [1], En-Tang Kang [2,*] and Liqun Xu [1,*]

[1] BRICS Joint Laboratory on Biomedical Materials, School of Materials and Energy, Southwest University, Chongqing 400715, China
[2] Department of Chemical and Biomolecular Engineering, National University of Singapore, Kent Ridge, Singapore 117576, Singapore
* Correspondence: sathegene@gmail.com (S.G.); cheket@nus.edu.sg (E.-T.K.); xulq@swu.edu.cn (L.X.)

How To Cite: Li, W.; Xiang, L.; Gnanasekar, S.; et al. Construction of AIE Molecule-Embedded Long-Persistent Luminescence Coating for Self-Activated Photodynamic Antibacterial Performance. *Advanced Antibacterial Materials* **2025**.

Received: 3 October 2025
Revised: 11 November 2025
Accepted: 25 November 2025
Published: 11 December 2025

Abstract: Photodynamic therapy (PDT) has emerged as a pivotal strategy for mitigating the risk of implant-associated infections (IAIs) due to its minimally invasive nature and the reduced emergence of multidrug-resistant (MDR) bacterial strains. However, the limited tissue penetration depth of visible light fundamentally constrains the therapeutic efficacy of PDT in deep-seated infections. Herein, we engineered a self-luminescent polydimethylsiloxane (PDMS) composite (PDMS-S) by integrating persistent luminescence material ($Sr_2MgSi_2O_7$: Eu^{2+}, Dy^{3+}). Simultaneously, we encapsulated an aggregation-induced emission luminogen (AIEgen; TTVP) with exceptional photosensitizing efficiency within a hybrid polymeric network of phytic acid (PA) and carboxymethyl chitosan (CMCS). The resulting PA-CMCS-TTVP (PA-CT) aggregates are conveniently deposited onto PDMS-S surfaces. The intrinsic luminescence of PDMS-S enabled the PA-CT coating to generate sustained reactive oxygen species (ROS), resulting in long-term effective PDT. This work significantly expands the biomedical applications of PDT and provides a transformative strategy for deep-tissue infections.

Keywords: phytic acid; carboxymethyl chitosan; antibacterial coating; self-illumination; AIE

1. Introduction

Preventing bacterial adhesion and colonization is considered a primary challenge in the engineering of biomedical implants with improved functionalities [1–4]. Implant surfaces are particularly vulnerable to polymicrobial infections, resulting in biofilm formation that compromises immune responses at the tissue-implant interface [5]. Once established, biofilms employ multiple mechanisms to shield embedded bacteria from both host defenses and antimicrobial agents, ultimately causing IAIs [6,7]. Since biofilms can form on virtually any surgical material, their prevention is critical for improving patient survival. This clinical necessity has driven the development of various antibacterial coating strategies [8].

Photodynamic therapy (PDT) has emerged as a widely adopted antibacterial strategy due to its unique advantages and minimal systemic toxicity, proving particularly effective against microbial infections [9]. Antibacterial photodynamic therapy (APDT) operates through an interactive mechanism where photosensitizers (PSs) generate reactive oxygen species (ROS) upon light irradiation, enabling bacterial growth inhibition or eradication. Importantly, recent studies have demonstrated the effectiveness of APDT against multidrug-resistant (MDR) strains without inducing bacterial resistance, which represents a significant advantage compared with

conventional antibiotics [10,11]. However, most clinically available PSs remain constrained by UV-visible spectral activation (<700 nm), exhibiting three fundamental limitations: (i) poor tissue penetration depth; (ii) rapid energy attenuation at longer wavelengths; and (iii) insufficient ROS generation for therapeutic effects [12]. Moreover, achieving optimal PDT efficacy typically requires prolonged light irradiation, which inevitably causes photothermal damage to surrounding healthy tissues due to the dissipation of energy. These issues severely restrict APDT's therapeutic potential in deep-seated infections [13,14].

Long-persistent luminescence (LPL) materials, also termed afterglow luminescent materials, exhibit a luminescence mechanism categorized under photoluminescence. Specifically, LPL materials store energy in excited states upon photoexcitation and gradually release this energy as light after excitation ceases. In 1996, Matsuzawa reported a europium (Eu)- and dysprosium (Dy)-doped strontium aluminate ($SrAl_2O_4$) system with an afterglow decay time exceeding 10 h and exceptional durability [15]. This discovery demonstrated the potential of LPL materials as internal light sources for PDT. Owing to their renewable optical energy storage capacity, LPL materials could be regarded as "rechargeable optical batteries", capable of activating PSs within biological tissues, thereby enabling PDT effects and addressing their limitations in deep-tissue therapeutic applications [16].

In this work, we incorporated $Sr_2MgSi_2O_7$: Eu^{2+}, Dy^{3+} (SMSO) into polydimethylsiloxane (PDMS) to fabricate a self-luminescent "PDMS optical battery" (PDMS-S) that emits prolonged blue fluorescence following UV charging at 365 nm. Our previous studies have shown that phytic acid (PA) can form an aggregate with carboxymethyl chitosan (CMCS) through electrostatic interactions and van der Waals forces, which rapidly deposit onto substrate surfaces to create polymeric network coatings [17–19]. Consequently, an aggregation-induced emission luminogen (AIEgen; TTVP) with blue-light absorption was incorporated into a polymeric network consisting of PA and CMCS. The as-formed PA-CMCS-TTVP (PA-CT) aggregates were deposited onto PDMS-S via gravitational effect and the surface adhesion of PA. The impact of PDMS-S luminescence (post-365 nm UV charging) on PA-CT-mediated ROS generation was evaluated. Additionally, its antibacterial efficacy was investigated *in vitro* and *in vivo* to establish a versatile strategy for addressing deep-tissue APDT challenges (Scheme 1).

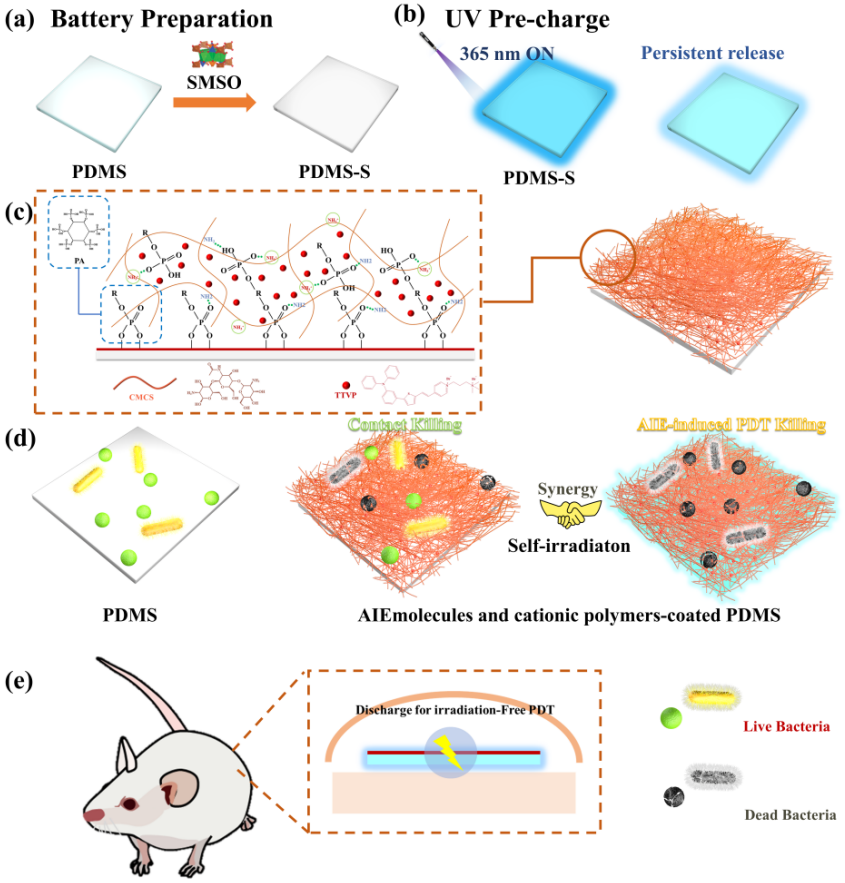

Scheme 1. (**a**) Schematic illustration of the fabrication of self-luminescent PDMS-S; (**b**) Persistent afterglow emission of PDMS-S following 365 nm UV charging; (**c**) Electrostatic interaction between PA and CMCS forming the polymeric network and encapsulating the AIEgen; (**d**) Dual antibacterial mechanism of the PA-CT coating through "contact-killing" and APDT-induced ROS generation; (**e**) *In vivo* intrinsic luminescence of PDMS-S in a rat model.

2. Experimental Section

2.1. Materials

CMCS (Product No.: C914893, M_w: 240 KDa, deacetylation degree > 90%, substitution degree 90%) was purchased from Shanghai Macklin Biochemical Technology Co., Ltd. (Shanghai, China). PA (70% in water) was purchased from J&K Scientific Ltd. (Beijing, China). PDMS prepolymer base agent (Sylgard 184A) and thermal curing agent (Sylgard 184B) were purchased from Dow Corning Corporation. *Escherichia coli* (*E. coli*, Type: CMCC 44102) and *Staphylococcus aureus* (*S. aureus*, Type: CMCC 26003) were obtained from the National Center for Medical Culture Collection. Methicillin-resistant *S. aureus* (MRSA, Type: ATCC 33592) was procured from the American Type Culture Collection. All other reagents were purchased from J&K Scientific Ltd. (Beijing, China), Sigma Aldrich Chemical Co. (Shanghai, China), Adamas Reagent Co., Ltd. (Shanghai, China), and Sangon Biotech Co., Ltd. (Shanghai, China). Deionized (DI) water was used throughout all experiments. TTVP was prepared according to the method reported in the literature [20].

2.2. Preparation of PDMS-S

For the preparation of PDMS-S, 30 mL of PDMS prepolymer solution was transferred to a centrifuge tube, followed by the addition of 3 mL of crosslinking agent. The mixture was then stirred vigorously until homogeneous mixing was achieved. Subsequently, 6 g of SMSO powder was incorporated into the mixture under rapid mechanical agitation for 30 min to ensure uniform dispersion within the PDMS matrix. The PDMS prepolymer-SMSO suspension was then allowed to rest for 2 h under static conditions to facilitate bubble removal. Finally, PDMS-S was cured and molded at room temperature.

2.3. Preparation of CMCS and TTVP (CT) Solution Mixture

Firstly, the CMCS (100 mg) was dissolved in 30 mL of DI water in a 100-mL round-bottom flask and vigorously stirred for 10 min to form a homogeneous solution. Then, TTVP (15 mg) was added to the CMCS solution and stirred continuously for an additional 24 h to obtain the CT solution.

2.4. Surface Deposition of the PA-CT Coating

A modified PDMS-S surface was prepared by depositing a PA-CT coating, which was formed by mixing 2 mL of the CT solution mixture with 1 mL of a PA aqueous solution (1 mg/mL). The PDMS-S were immersed in the PA-CT suspension for 3 h, and modified substrates were washed with DI water, followed by drying at room temperature.

Additional information on the experimental methods can be found in the Supplementary Materials.

3. Results and Discussion

SMSO powder was added to PDMS prepolymer for PDMS-S fabrication with persistent luminescence (Figure 1a). After charging with a 365 nm UV lamp, PDMS-S emitted intense blue fluorescence visible to the naked eye upon cessation of irradiation (Figure 1b) [21]. The emission spectrum of PDMS-S was observed using a fluorescence spectrophotometer, revealing a maximum emission wavelength at 478 nm (Figure 1c). The persistent luminescence performance of PDMS-S was also tested, showing that PDMS-S emitted high-intensity blue light signals within 20 min and continued to emit instrument-detectable blue fluorescence for at least 2 h thereafter (Figure 1d). This characteristic indicates the remarkable LPL properties of PDMS-S, which are beneficial for prolonged APDT. We systematically investigated the impact of charging time on the luminescence performance of PDMS-S. As depicted in Figure 1e, the onset of high-intensity blue light emission from PDMS-S was significantly delayed with increased charging time. After 15 min of charging, the duration of high-intensity blue fluorescence emission from PDMS-S extended to 28 min. Our results suggest that increased charging time enhances the luminescence performance of PDMS-S, indicating a substantial positive association between these two factors. Due to its excellent mechanical properties, resistance to biodegradation, biocompatibility, and chemical stability, the PDMS elastomer is widely explored for engineering advanced functional biomaterials [22]. In this work, we studied the impact of SMSO incorporation on the mechanical properties of PDMS-S. The stress-strain curves and resilience curves of pristine PDMS and PDMS-S were nearly identical (Figure 1f,g), which indicates that the incorporation of SMSO does not significantly alter the mechanical properties of PDMS-S.

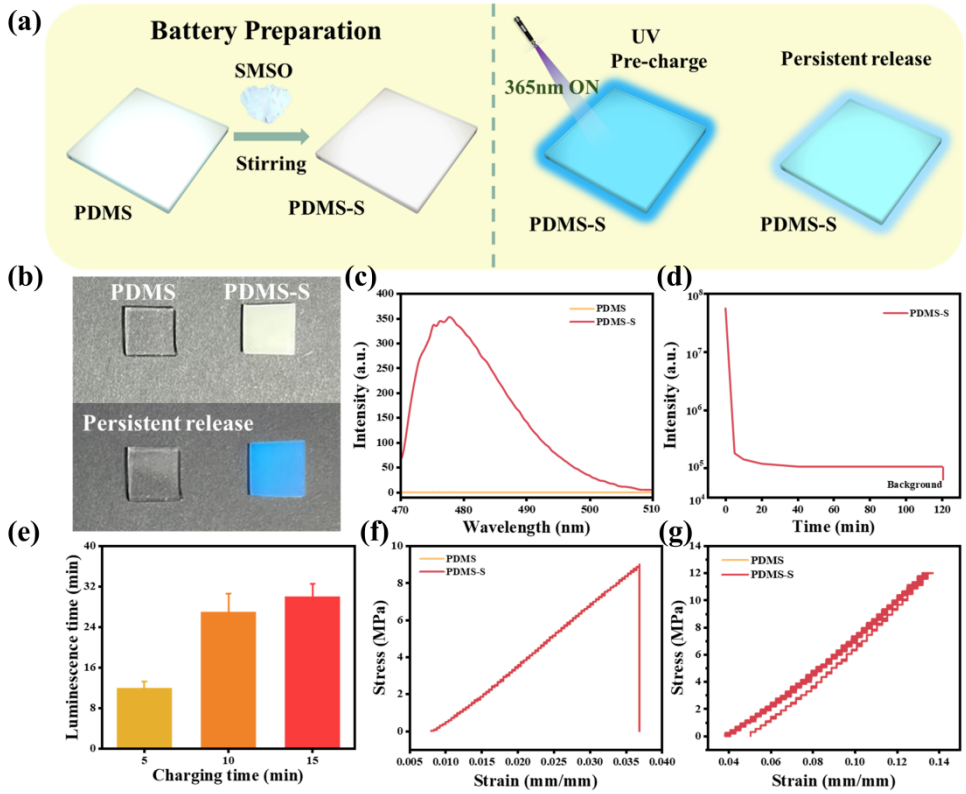

Figure 1. (**a**) Schematic illustration of the LPL phenomenon of PDMS-S; (**b**) Digital photograph of PDMS-S exhibiting bright blue afterglow emission after 365 nm UV charging; (**c**) Photoluminescence (PL) spectra of pristine PDMS and PDMS-S; (**d**) Afterglow decay curve of PDMS-S; (**e**) Effect of charging duration on the persistence of PDMS-S emission; (**f**) Stress-strain curves and (**g**) resilience curves of PDMS and PDMS-S.

TTVP was dissolved in an aqueous CMCS solution under continuous stirring for 12 h to obtain a homogeneous CT mixture. Further, the UV-visible absorption spectra displayed negligible absorption in the 300–700 nm range for the CMCS solution, whereas TTVP exhibited a strong absorption peak at 480 nm. Similarly, the CT suspension exhibited a slightly red-shifted absorption maximum at 497 nm, indicating minimal alteration of optical characteristics upon CMCS incorporation (Figure 2a). Although both PA and CT solutions were transparent, their mixture immediately turned turbid (Figure S1). From the zeta potential measurements, it was noticed that the contrasting surface charges of PA (−4.81 V) and CT (+22.03 V) (Figure 2b) facilitate the electrostatic attraction between the phosphate groups of PA and the amino groups in CMCS. Dynamic light scattering (DLS) analysis also confirmed the formation of PA and CT aggregation in aqueous solution (Figure 2c). Furthermore, the PA-CT solution generates a dramatically reduced transmittance (merely 1%) across the 350–600 nm spectral range (Figure 2d). In the emission spectral measurements, the fluorescence intensity of the PA-CT aggregates was 80 and 73 times higher than that of CMCS and CT, respectively, under 480 nm excitation (Figure 2g,f). Collectively, these findings imply the successful encapsulation of TTVP within the PA-CMCS polymeric network, which confers pronounced AIE characteristics.

By recording the maximum encapsulation efficiency of TTVP in PA-CMCS with a concentration increment test (0.05 mg/mL increments), the optimal encapsulation concentration of TTVP (0.5 mg/mL) was determined (Figure 3a). The native PDMS surface lacks functional group binding sites for PA, which hinders the PA-CT coating formation on the PDMS-S surface. Plasma treatment oxidizes the O-Si$(CH_3)_2$ molecules on the PDMS-S surface to form hydroxyl groups, resulting in enhanced bonding forces between PA and PDMS. This modification significantly enhanced the bonding of PA-CT to the PDMS surface, enabling the uniform deposition of PA-CT on the PDMS-S surface (Figure 3b,c). As shown in Figure 3d, the field-emission scanning electron microscopic (FESEM) images of unmodified PDMS-S surfaces exhibited pronounced wrinkling artifacts induced by electron beam bombardment. In contrast, the PDMS-S@PA-CT surface is entirely devoid of such features, indicating that the dense PA-CT coating covers the PDMS-S surface. In the X-ray photoelectron spectroscopic (XPS) wide-scan spectra, the appearance of P 2p and P 2s, along with the disappearance of Si 2p and Si 2s signals for PDMS-S@PA-CT, depicts PA-CT deposition (Figure 3e). The cross-sectional morphology of the PA-CT coating was much thicker than that of the PA-CMCS coating, attributed to the increased particle size by TTVP addition (Figure 3f).

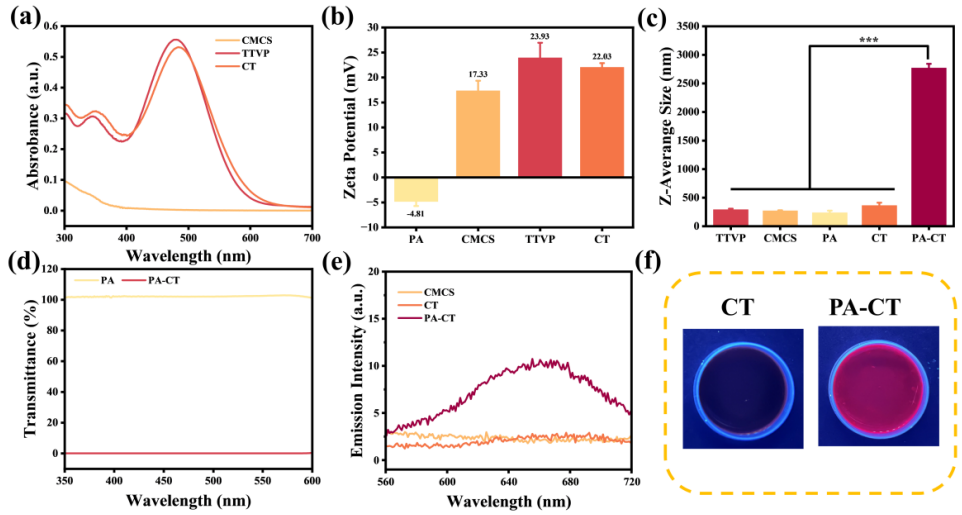

Figure 2. (**a**) UV-visible absorption spectra of TTVP, CMCS, and CT solutions; (**b**) Zeta potentials of PA, TTVP, CMCS, and CT; (**c**) DLS profiles of PA, TTVP, CMCS, CT, and PA-CT; (**d**) Optical transmittance of PA and PA-CT; (**e**) PL spectra of CMCS, CT, and PA-CT under 480 nm excitation; (**f**) Photographs of CT and PA-CT suspensions under UV illumination. *** $p < 0.001$.

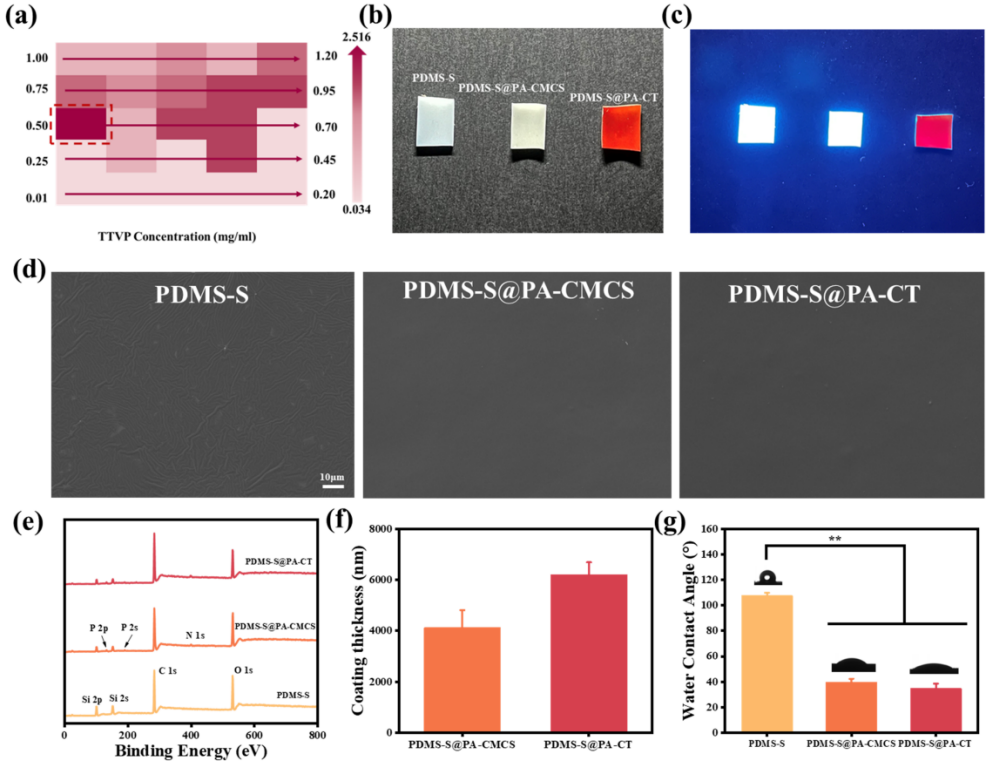

Figure 3. (**a**) Optimization of TTVP encapsulation concentration in the PA-CMCS network; (**b**) Photographs of pristine, plasma-treated, and PA-CT-coated PDMS-S substrates; (**c**) Photographs of PDMS-S and PDMS-S@PA-CT under UV illumination; (**d**) FESEM images of PDMS-S and PDMS-S@PA-CT surfaces; (**e**) XPS wide-scan spectra of PDMS-S, PDMS-S@PA-CMCS, and PDMS-S@PA-CT; (**f**) Cross-sectional thickness of PA-CMCS and PA-CT coatings; (**g**) WCAs of PDMS-S, PDMS-S@PA-CMCS, and PDMS-S@PA-CT. ** $p < 0.01$.

PDMS is a hydrophobic elastomer, polar solvents (e.g., water) have difficulty wetting this surface [23]. Due to the importance of surface wettability in designing biointerfaces and developing functional biomaterials, it can significantly reduce the frictional resistance of materials during implantation, thereby improving the biocompatibility of medical implants. By regulating surface wettability, the interaction of biomedical implants with tissues can be optimized to enhance their clinical performance and long-term stability [24]. The water contact angle (WCA) of PDMS-S was significantly reduced after modification by PA-CT coating (Figure 3g). This phenomenon is manifested

by the fact that the CMCS molecule contains a large number of hydrophilic groups, such as amino and hydroxyl groups [25,26], which significantly enhance the hydrophilicity of the PA-CT coating.

Furthermore, the energy band structure of PA-CT coatings was systematically investigated by measuring the valence band (VB) position (E_v) using VB XPS. Initially, a horizontal extension line was generated at 0 eV of the VB XPS test data, and the E_v value was determined by the intersection of the tangent line in the curve with this extension line (Figure 4b). Subsequently, the forbidden bandwidth (E_g) of the PA-CT coating was determined by UV diffuse reflectance spectroscopy (UV-DRS). The UV-DRS data were converted to Tauc plots using the Kubelka-Munk equation, and a tangent line was drawn at the extreme point of the curve. The intersection of the tangent line and the horizontal coordinate represented the E_g value (Figure 4a). Based on the E_g and E_v values, the conduction band position (E_c) of the PA-CT coating was further calculated [27,28]. As illustrated in Figure 4c, we mapped the energy band structure of the PA-CT coating using the obtained data and predicted that the PA-CT coating can generate both singlet oxygen ($^1O_2$) and hydroxyl radical (·OH) ROS. The ROS-generating ability of PA-CT coatings was examined using methylene blue (MB) and 9,10-anthracenediyl-bis(methylene)dicarboxylic acid (ABDA) as indicators. After 365 nm UV light irradiation, the PDMS-S@PA-CT immersed in the ABDA solution exhibits a variation in the absorbance recorded at 400 nm. The UV-Vis spectroscopic analysis explicitly demonstrates a significant decrease in absorbance (Figure 4d) due to the interaction of ABDA with ROS and a photobleaching effect [29]. In addition, the decomposition rates showed that only PDMS-S@PA-CT charged by 365 nm UV light exhibits a significant decomposition of ABDA. The PL of PDMS-S effectively activates TTVP in the PA-CT coating, triggering ROS generation and oxidized ABDA solution (Figure 4f). Likewise, the ROS-generating ability of PDMS-S@PA-CT in MB solution [30]. shows the same trend of MB decomposition rate under the charge of 365 nm UV light (Figure 4e,g). An electron paramagnetic resonance (ESR) spectroscopic measurement of PDMS-S@PA-CT exposed to 5,5-dimethyl-1-pyrroline-*N*-oxide (DMPO) and 2,2,6,6,-tetramethyl-4-piperidinol (TEMP) has been used for the detection of ROS [31]. It was observed that the PDMS-S@PA-CT charged by 365 nm UV light generated significant signals of ·OH and $^1O_2$ (Figure 4h,i), which corroborates our theoretical calculations of the energy band structure of the PA-CT coating. It was convincingly proven that the blue fluorescence emitted by PDMS-S can excite TTVP in the PA-CT coating and produce ROS [32].

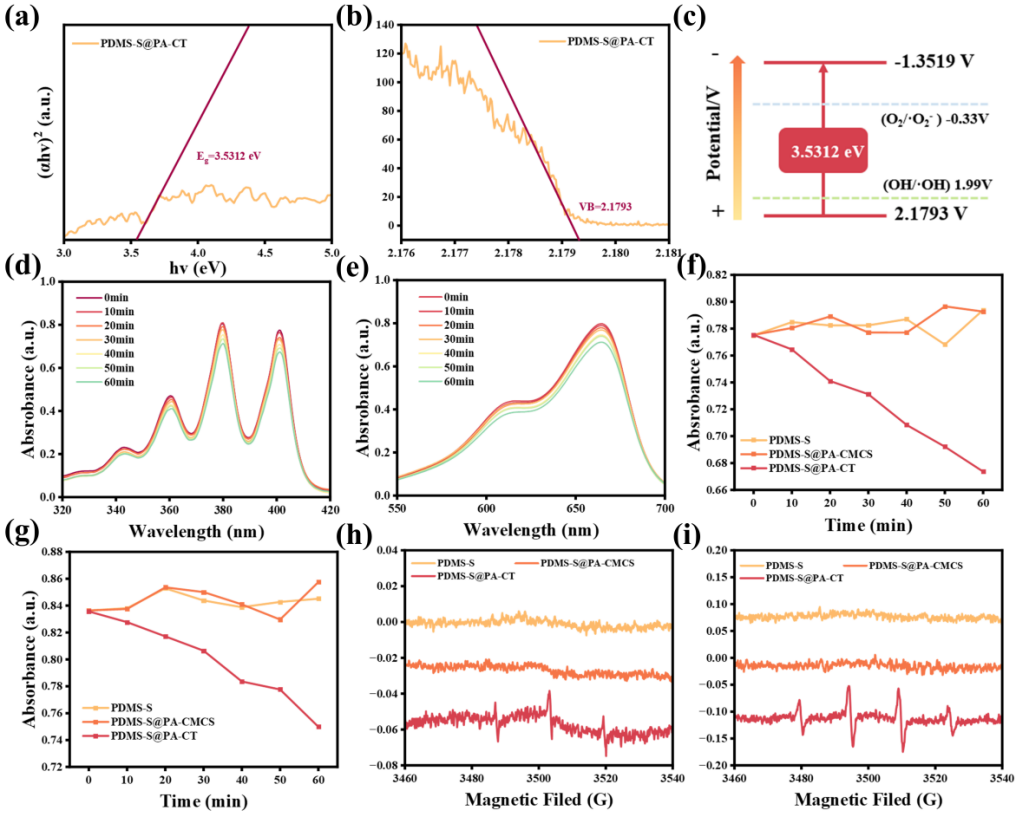

Figure 4. (**a**) UV-DRS and corresponding Tauc plot of PA-CT; (**b**) VB XPS spectrum of PA-CT; (**c**) Schematic energy band structure of PA-CT; (**d**,**e**) Time-dependent degradation curves of ABDA and MB, respectively, under 365 nm irradiation with PDMS-S@PA-CT; (**f**) Absorbance decay of ABDA at 400 nm and (**g**) MB at 665 nm; (**h**) ESR signal of $^1O_2$ using TEMP; (**i**) ESR signal of ·OH using DMPO for PDMS-S, PDMS-S@PA-CMCS, and PDMS-S@PA-CT substrates.

The antibacterial efficiencies of the PA-CT coating against *S. aureus*, *E. coli*, and MRSA were assessed by the spread plate method after co-culturing the pristine and modified PDMS-S substrates with bacterial suspensions. As depicted in Figure 5a,b, PDMS-S@PA-CMCS exhibited a moderate "contact-killing" effect due to the electrostatic interaction between the amino group in CMCS and the negatively charged bacterial membrane [33,34]. Since TTVP contains positively-charged quaternary ammonium groups in an aqueous medium, it easily adsorbs onto the bacterial surface and penetrates the cell wall. It is hoped that damaging the bacterial cell membrane impedes regular ion exchange and disrupts protoplasmic membrane permeability, resulting in intracellular leakage and bacterial cell death [35,36]. Therefore, the modified PDMS-S@PA-CT substrates exhibited intrinsic antimicrobial activity even in the absence of UV light treatment. Upon 365 nm UV irradiation, the PDMS-S@PA-CT produces ROS and exhibits a synergistic elimination of almost 99.99% of *S. aureus* and 91.71% of *E. coli* (Figure 5c,d). Meanwhile, FESEM was used to observe the morphological alterations of bacteria on the surface of pristine and modified substrates. It can be visualized that the bacteria on the pristine PDMS-S surface maintained a rounded and intact morphology, whereas the bacteria adhered to the PDMS-S@PA-CT surface showed a crumpled morphology with a reptured structure. The intrinsic bactericidal effect of PDMS-S@PA-CT denotes its promising "contact-killing" effect. Exposure to 365 nm UV light resulted in the complete rupture of the cell membrane and loss of its original structure (Figure 5e,f).

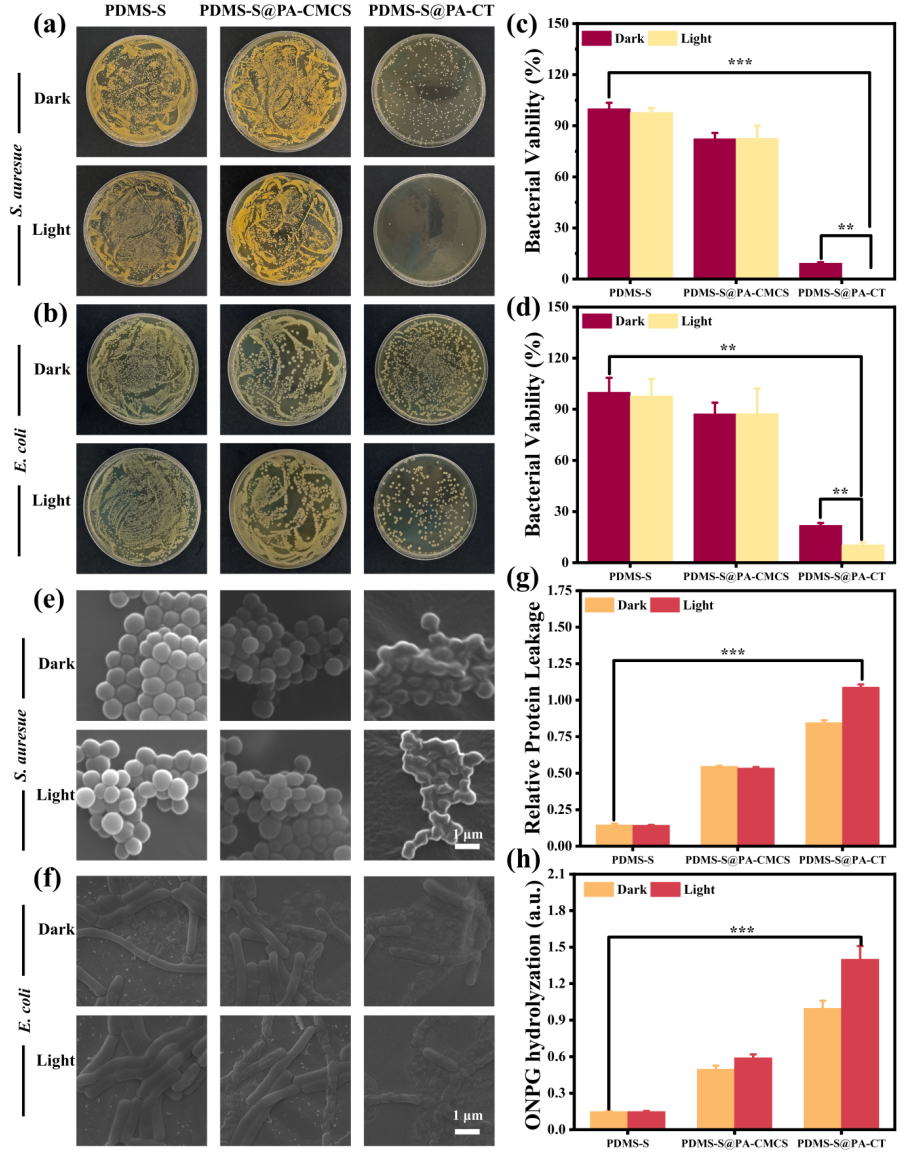

Figure 5. Antibacterial performance of pristine and modified PDMS-S substrates. (**a**,**b**) Digital photographs of tryptic soy broth (TSB)-agar plates inoculated with *S. aureus* and *E. coli* detached from different substrates; (**c**,**d**) Quantification of viable *S. aureus* and *E. coli* cells; (**e**,**f**) FESEM images of bacterial morphology on pristine PDMS-S and PDMS-S@PA-CT surfaces; (**g**) Protein leakage detected by BCA assay and (**h**) ONPG hydrolysis of *S. aureus* after treatment with different substrates, with or without 365 nm UV irradiation. ** $p < 0.01$, *** $p < 0.001$.

To explore the antibacterial mechanism, the *o*-nitrophenyl-*β*-D-galactopyranoside (ONPG) hydrolysis activity and bicinchoninic acid (BCA) protein assay kit of *S. aureus* before and after 365 nm UV light irradiation were studied [37]. The experimental results showed that the concentration of *o*-nitrophenol produced by the PDMS-S@PA-CT-treated bacteria was significantly higher than that of the original PDMS-S-treated bacteria. This phenomenon was further exacerbated when PDMS-S@PA-CT was charged by 365 nm UV light, indicating that PDMS-S@PA-CT had more significant disruptive effects on bacterial cell membranes under photoexcitation. The results of the BCA experiments were similar to those of the ONPG experiments, where an increased cytoplasmic protein release has been recorded in bacteria treated with PDMS-S@PA-CT compared to the pristine PDMS-S. These differences were further amplified after exposure to light (Figure 5g,h). The emergence of bacterial resistance to antibiotics is a growing concern and poses a significant global health challenge [38]. As a result, the synergistic antimicrobial effectiveness of PDMS-S@PA-CT against MRSA was assessed to establish potential antibacterial strategies. Our results show that PDMS-S@PA-CT charged by 365 nm UV light had significant antimicrobial effects on MRSA (Figure S2). Additionally, the PA-CT coating was evaluated for its ability to inhibit the growth of bacterial biofilms. In the confocal laser scanning microscopic (CLSM) image of the pristine PDMS-S surface, the emission of a strong green fluorescence signal indicates that there was almost no bacterial death. On the other hand, a red fluorescence signal was observed for biofilms grown on PDMS-S@PA-CT, representing its "contact-killing" effect. Almost completely red fluorescent signals were observed on the surface biofilm of PDMS-S@PA-CT after exposure to 365 nm UV light, indicating that PDMS-S@PA-CT had a nearly 100% bacterial killing rate due to synergistic antimicrobial effects and demonstrated a good ability to inhibit biofilm formation (Figure S3).

An *in vivo* fluorescence imaging was adopted to evaluate the luminescence of PDMS-S@PA-CT in Sprague-Dawley (SD) rats. After implantation, the PDMS-S@PA-CT was charged by 365 nm UV light to record its luminescence effect in real time. As shown in Figure 6a, the obvious luminescent signals could be detected in rats within 30 min and weakened gradually with prolonged treatment. A certain intensity of the luminescence signal was still observable at 60 min, whereas the luminescence signal had almost disappeared in rats by 120 min. Therefore, we believe that PDMS-S@PA-CT can achieve a 30-min high-intensity APDT in rats, and the overall treatment effect can last for nearly 2 h.

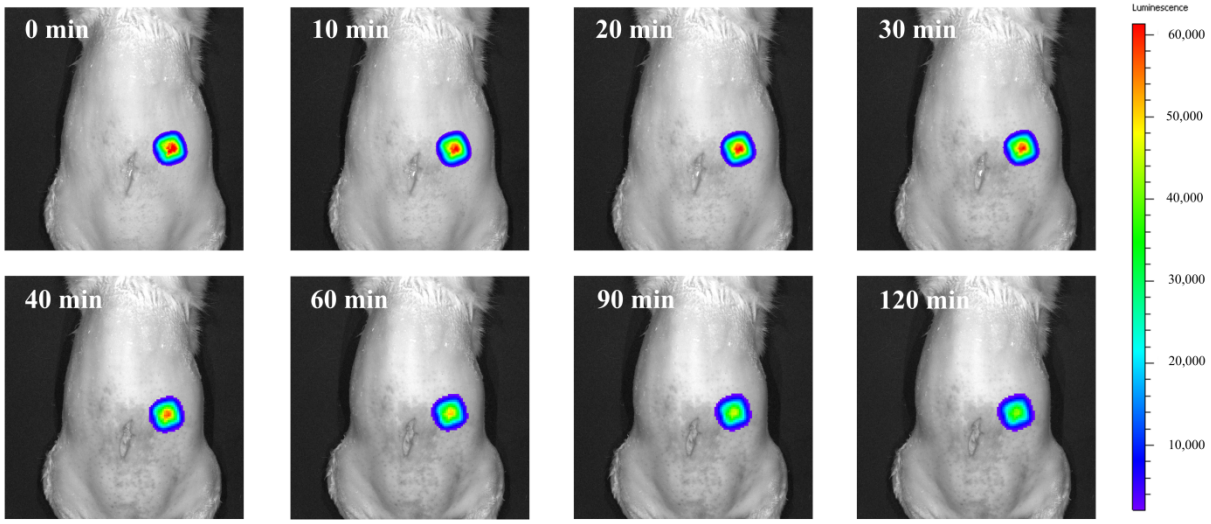

Figure 6. *In vivo* fluorescence imaging of PDMS-S@PA-CT implanted in SD rats after 365 nm UV charging.

Biocompatibility is a crucial parameter for implantable biomaterials, as it directly affects the long-term stability and safety [39]. After co-culturing with pristine and modified PDMS-S surfaces for 48 h, the survival rate of L929 cells on the modified PDMS-S surface exceeded 93% (Figure S4). Likewise, red blood cells (RBCs) immersed in pristine and modified PDMS-S substrates at 37 °C for 2 h revealed no significant hemolytic behavior (Figure S5).

A rat subcutaneous infection model was developed to assess the self-activated APDT and synergistic bactericidal action of the PDMS-S@PA-CT *in vivo*. The pristine and modified PDMS-S substrates were implanted beneath the dorsal skin of SD rats, followed by inoculation with *S. aureus* (1×10^8 cell/mL). Afterward, the SD rats were fed for a week and then sacrificed, and the implants were retrieved. The adhered bacteria on the implants were recovered and quantified by serial dilution and culturing on TSB-agar plates. As shown in Figure 7a, a large number of viable bacteria remained on the surface of the pristine PDMS-S, while the number of bacteria on the

surface of the PDMS-S@PA-CT was significantly reduced. Moreover, there is almost no viable bacteria recovered on the surface of PDMS-S@PA-CT after exposure to 365 nm UV light (Figure 7b). We also performed blood analysis comparing blood from rats implanted with PDMS-S@PA-CT to blood from rats implanted with pristine PDMS-S. The experimental results showed that the contents of RBCs, white blood cells (WBCs), and platelet components in all sample groups were within the normal range [40], similar to those of healthy rats (Figure 7c). In hematoxylin & eosin (H&E) staining, the skin tissues of pristine PDMS-S implanted rats have shown a significantly larger number of infiltrated inflammatory cells as compared with PDMS-S@PA-CT implanted groups. Interestingly, no inflammatory cells were observed at the PDMS-S@PA-CT implantation site after exposure to 365 nm UV light (Figure 7d). This suggests that PDMS-S@PA-CT exhibits good biocompatibility and effectively eliminates bacteria with minimal or no adverse inflammatory effects after 365 nm UV light irradiation.

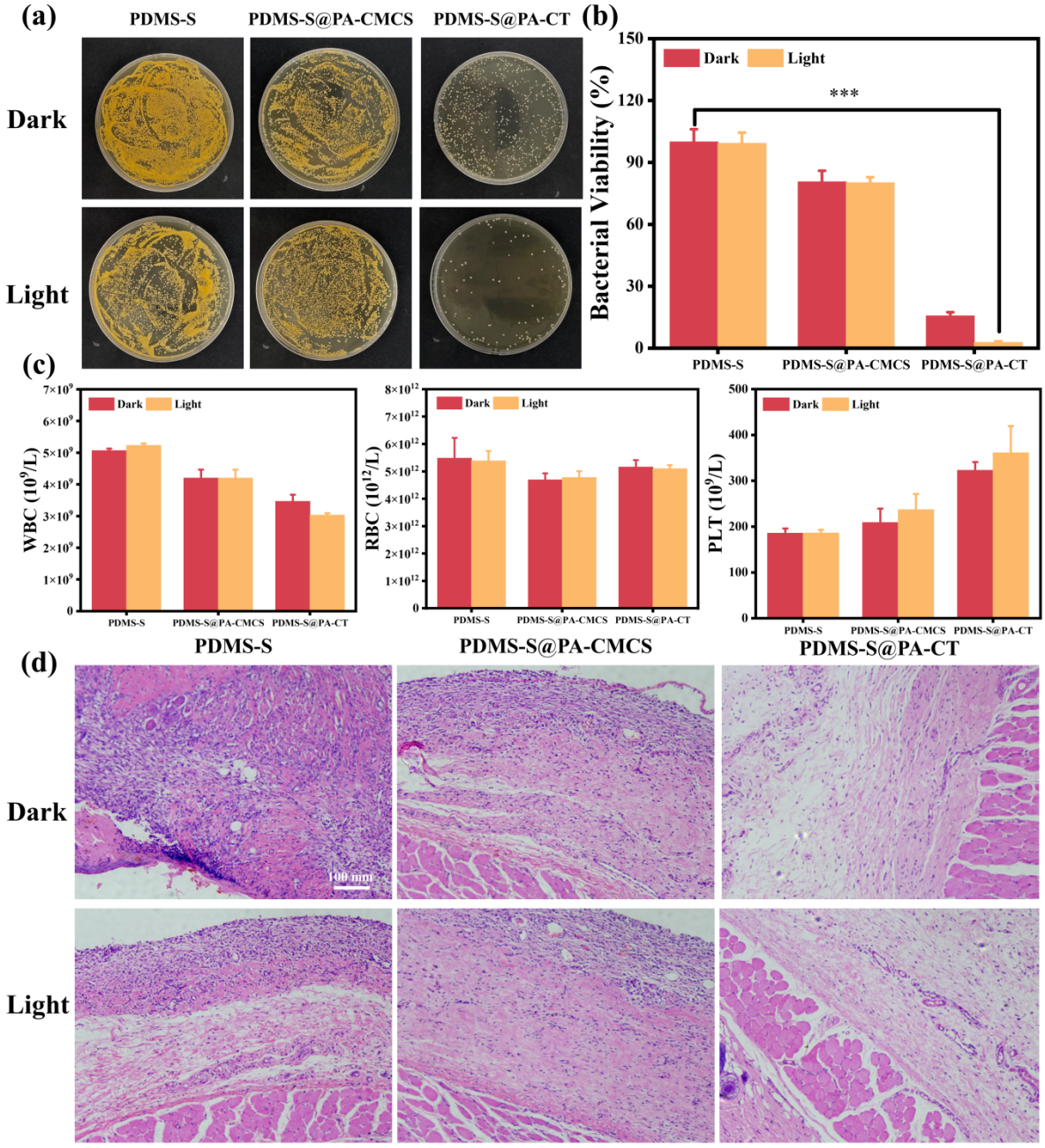

Figure 7. (**a**) Photographs of TSB-agar plates showing *S. aureus* colonies detached from pristine and modified PDMS-S implants retrieved from rat subcutaneous infection models; (**b**) Quantitative analysis of viable *S. aureus* on pristine and modified PDMS-S substrates with or without 365 nm UV charging; (**c**) Blood composition analysis (RBCs, WBCs, and platelets) of SD rats after implantation of pristine or modified PDMS-S; (**d**) H&E-stained sections of rat skin tissue adjacent to implants one week post-implantation. *** $p < 0.001$.

4. Conclusions

In this study, we developed a PDMS-S with long afterglow properties that actively emits blue fluorescence visible to the naked eye after being charged with 365 nm UV light. With the uniform AIE (PA-CT) deposition onto the PDMS-S surface, exploiting the surface adhesion and gravitational effect of PA supports the formation of a highly stable coating. The PA-CT-modified surface of PDMS-S exhibits potent antibacterial properties due to its blue fluorescence emission, which stimulates the AIE effect of TTVP aggregates within the PA-CMCS and generates excessive ROS. The as-designed PDMS-S@PA-CT coating prevents bacterial adhesion and biofilm formation by enabling "contact-killing" and the self-activated APDT. Additionally, the PDMS-S@PA-CT convincingly demonstrated excellent biocompatibility and anti-infective properties in a rat subcutaneous implantation model. Harnessing PDMS-S with rechargeable and self-activated APDT mitigates the existing hurdles in photodynamic bacterial inactivation, offering a novel strategy with pre-clinical prominence to combat bacterial infections.

Supplementary Materials

The additional data and information can be downloaded at: https://media.sciltp.com/articles/others/25121115 33487972/AAM-25110009-Supplementary-Materials-FC-done.pdf. Figure S1: Digital photographs of aqueous PA, CT, and their mixture (PA-CT). Figure S2: Antibacterial activity of PDMS-S@PA-CT against MRSA. (**a**) Photographs of TSB-agar plates inoculated with MRSA detached from pristine and modified PDMS-S surfaces; (**b**) Quantification of viable MRSA cells on different substrates. Figure S3: *S. aureus* and *E. coli* biofilms inhibition on pristine and modified PDMS-S substrates observed by CLSM. Figure S4: Cell viability of L929 fibroblasts cultured on pristine PDMS-S, PDMS-S@PA-CMCS, and PDMS-S@PA-CT substrates for 48 h. Figure S5: Hemolysis assay of pristine PDMS-S, PDMS-S@PA-CMCS, and PDMS-S@PA-CT substrates after incubation with RBCs for 2 h. *** $p < 0.001$.

Author Contributions

W.L.: conceptualization, methodology, writing—original draft preparation; L.X.: data curation, investigation, visualization; S.G.: project administration, writing—reviewing and editing; X.H.: data curation, investigation, visualization; Y.X.: methodology, investigation; K.X.: project administration; X.R.: project administration; E.-T.K.: supervision, funding acquisition, writing—reviewing and editing; L.X.: conceptualization, supervision, writing—reviewing and editing. All authors have read and agreed to the published version of the manuscript.

Funding

This research was supported by the National Key R&D Programmes of China (2022YFE0140300), National Natural Science Foundation of China (U24A20511, and 22378335), Fundamental Research Funds for the Central Universities (SWU-XJPY202304), and Chongqing Engineering Research Center for Micro-Nano Biomedical Materials and Devices.

Institutional Review Board Statement

The animal study was approved by the Animal Use and Care Committee of Southwest University (UCUCA) (Ethical Approval Number: IACUC-20220607-03).

Informed Consent Statement

Not applicable.

Data Availability Statement

The experimental data that support the findings of this study are available from the corresponding authors, upon reasonable request.

Conflicts of Interest

The authors declare no conflict of interest.

Use of AI and AI-Assisted Technologies

During the preparation of this work, the authors used ChatGPT to polish the language. After using this tool, the authors reviewed and edited the content as needed and takes full responsibility for the content of the published article.

References

1. Fu, J.; Wang, C.; Mao, C.; et al. Bacteria-Powered Photodynamic Amplification on Nano-Bio Interface for Selective Pathogen Killing and Tissue Regeneration. *Adv. Antibact. Mater.* **2025**. Available online: https://www.sciltp.com/journals/aam/articles/2507000989 (accessed on 3 November 2025).
2. Rooney, L.J.; Marshall, A.; Tunney, M.M.; et al. Phenylboronic Acid-Modified Polyethyleneimine: A Glycan-Targeting Anti-Biofilm Polymer for Inhibiting Bacterial Adhesion to Mucin and Enhancing Antibiotic Efficacy. *ACS Appl. Mater. Interfaces* **2025**, *17*, 19276–19285.
3. Zhang, X.; Wang, Y.; Yang, C.; et al. Cu-Bearing Antibacterial Stainless Steel Potentiates Antibiotic Sensitivity to Combat *Methicillin-resistant Staphylococcus aureus*. *Adv. Antibact. Mater.* **2025**. Available online: https://www.sciltp.com/journals/aam/articles/2509001365 (accessed on 3 November 2025).
4. Ziegelmeyer, T.; de Sousa, K.M.; Liao, T.-Y.; et al. Multifunctional micro/nano-textured titanium with bactericidal, osteogenic, angiogenic and anti-inflammatory properties: Insights from *in vitro* and *in vivo* studies. *Mater. Today Bio* **2025**, *32*, 101710.
5. Tan, L.; Li, J.; Liu, X.; et al. Rapid biofilm eradication on bone implants using red phosphorus and near-infrared light. *Adv. Mater.* **2018**, *30*, 1801808.
6. Jiang, F.; Wang, J.; Ren, Z.; et al. Targeted light-induced immunomodulatory strategy for implant-associated infections via reversing biofilm-mediated immunosuppression. *ACS Nano* **2024**, *18*, 6990–7010.
7. Wang, J.; Wang, L.; Pan, J.; et al. Magneto-based synergetic therapy for implant-associated infections via biofilm disruption and innate immunity regulation. *Adv. Sci.* **2021**, *8*, 2004010.
8. Chen, X.; Zhou, J.; Qian, Y.; et al. Antibacterial coatings on orthopedic implants. *Mater. Today Bio* **2023**, *19*, 100586.
9. Gnanasekar, S.; Kasi, G.; He, X.; et al. Recent advances in engineered polymeric materials for efficient photodynamic inactivation of bacterial pathogens. *Bioact. Mater.* **2023**, *21*, 157–174.
10. Li, L.; Wang, Y.; Huang, T.; et al. Cationic porphyrin-based nanoparticles for photodynamic inactivation and identification of bacteria strains. *Biomater. Sci.* **2022**, *10*, 3006–3016.
11. Xia, F.W.; Guo, B.W.; Zhao, Y.; et al. Type I photosensitizer targeting glycans: Overcoming biofilm resistance by inhibiting the two-component system, quorum sensing, and multidrug efflux. *Adv. Mater.* **2023**, *35*, 2309797.
12. Tsay, J.M.; Trzoss, M.; Shi, L.; et al. Singlet oxygen production by peptide-coated quantum dot—photosensitizer conjugates. *J. Am. Chem. Soc.* **2007**, *129*, 6865–6871.
13. Shen, Y.; Shuhendler, A.J.; Ye, D.; et al. Two-photon excitation nanoparticles for photodynamic therapy. *Chem. Soc. Rev.* **2016**, *45*, 6725–6741.
14. Zhan, Q.; Qian, J.; Liang, H.; et al. Using 915 nm laser excited $Tm^{3+}/Er^{3+}/Ho^{3+}$-doped NaYbF4 upconversion nanoparticles for *in vitro* and deeper *in vivo* bioimaging without overheating irradiation. *ACS Nano* **2011**, *5*, 3744–3757.
15. Kabe, R.; Adachi, C. Organic long persistent luminescence. *Nature* **2017**, *550*, 384–387.
16. Hu, L.; Wang, P.; Zhao, M.; et al. Near-infrared rechargeable "optical battery" implant for irradiation-free photodynamic therapy. *Biomaterials* **2018**, *163*, 154–162.
17. He, X.; Wu, H.; Xu, K.; et al. Biomimetic Engineering of Robust Gradient Antibacterial Coatings using Hollow Nanoframes of Prussian Blue Analogues. *Adv. Mater.* **2025**, *37*, 2501174.
18. Jiang, Y.; He, X.; Xiang, L.; et al. Phytic Acid-Polypeptide Network-Promoted Deposition of Photoactive Agents for the Construction of Synergistic Bactericidal Coatings. *ACS Appl. Mater. Interfaces* **2025**, *17*, 36260–36272.
19. Li, W.; Xiang, L.; Liu, Y.; et al. Construction of natural AIEgens-embedded chitosan network coatings with synergistic antibacterial effects. *Surf. Coat. Technol.* **2025**, *498*, 131814.
20. Wang, D.; Su, H.; Kwok, R.T.; et al. Rational design of a water-soluble NIR AIEgen, and its application in ultrafast wash-free cellular imaging and photodynamic cancer cell ablation. *Chem. Sci.* **2018**, *9*, 3685–3693.
21. Sampaio, D.; Souza, N.; Santos, J.; et al. Translucent and persistent luminescent $SrAl_2O_4$: Eu^{2+} Dy^{3+} ceramics. *Ceram. Int.* **2016**, *42*, 4306–4312.
22. Li, S.; Zhang, J.; He, J.; et al. Functional PDMS elastomers: Bulk composites, surface engineering, and precision fabrication. *Adv. Sci.* **2023**, *10*, 2304506.
23. Kim, G.; Jin, S. Hydrochannel-containing hydrophobic polymers by inverse emulsion polymerization for moisture-driven actuators. *ACS Appl. Mater. Interfaces* **2020**, *12*, 55223–55230.
24. Meng, J.; Yang, G.; Liu, L.; et al. Cell adhesive spectra along surface wettability gradient from superhydrophilicity to superhydrophobicity. *Sci. China Chem.* **2017**, *60*, 614–620.

25. Li, H.; Long, M.; Su, H.; et al. Carboxymethyl chitosan assembled piezoelectric biosensor for rapid and label-free quantification of immunoglobulin Y. *Carbohydr. Polym.* **2022**, *290*, 119482.
26. Liang, D.; Tang, J.; Sun, Q.; et al. Achieving ultra-low latent heat of water evaporation in capillary water by regulating hydrophilic groups and pore structure of cellulose/chitosan gel. *Carbohydr. Polym.* **2025**, *353*, 123302.
27. Christy, A.A.; Kvalheim, O.M.; Velapoldi, R.A. Quantitative analysis in diffuse reflectance spectrometry: A modified Kubelka-Munk equation. *Vib. Spectrosc.* **1995**, *9*, 19–27.
28. Wang, W.-Y.; Chiou, J.-C.; Chen, W.-X.; et al. Biosafety evaluation and quantitative determination of poly (hexamethylene biguanide)(PHMB) coated on cellulosic fabrics by Kubelka–Munk equation. *Cellulose* **2021**, *28*, 6651–6661.
29. Jia, L.; Zhou, Z.; Li, X.; et al. A multifunctional ROS cascade nanoplatform enables common prosperity of O_2 and H_2O_2 for magnetic targeting and fluorescence imaging-guided photodynamic/chemodynamic therapy. *Chem. Eng. J.* **2025**, *506*, 160178.
30. Chatterjee, A.; Sharma, A.K.; Purkayastha, P. Development of a carbon dot and methylene blue NIR-emitting FLIM-FRET pair in niosomes for controlled ROS generation. *Nanoscale* **2022**, *14*, 6570–6584.
31. D'Errico, G.; Vitiello, G.; De Tommaso, G.; et al. Electron Spin Resonance (ESR) for the study of Reactive Oxygen Species (ROS) on the isolated frog skin (*Pelophylax bergeri*): A non-invasive method for environmental monitoring. *Environ. Res.* **2018**, *165*, 11–18.
32. Yu, Y.; Wu, S.; Zhang, L.; et al. Cationization to boost both type I and type II ROS generation for photodynamic therapy. *Biomaterials* **2022**, *280*, 121255.
33. Huang, G.; Li, Y.; Qin, Z.; et al. Hybridization of carboxymethyl chitosan with MOFs to construct recyclable, long-acting and intelligent antibacterial agent carrier. *Carbohydr. Polym.* **2020**, *233*, 115848.
34. Zhang, M.; Yang, M.; Woo, M.W.; et al. High-mechanical strength carboxymethyl chitosan-based hydrogel film for antibacterial wound dressing. *Carbohydr. Polym.* **2021**, *256*, 117590.
35. Andreica, B.-I.; Mititelu-Tartau, L.; Rosca, I.; et al. Biocompatible hydrogels based on quaternary ammonium salts of chitosan with high antimicrobial activity as biocidal agents for disinfection. *Carbohydr. Polym.* **2024**, *342*, 122389.
36. Peng, G.; Hu, J.; Guo, J.; et al. Injectable exosome-loaded quaternized chitosan/oxidized sodium alginate hydrogel with self-healing, bioadhesive, and antibacterial properties for treating combined radiation-wound injury. *Chem. Eng. J.* **2024**, *494*, 152933.
37. Wu, J.; Shen, P.; Qin, X.; et al. Self-supply of H_2O_2 and O_2 by a composite nanogenerator for chemodynamic therapy/hypoxia improvement and rapid therapy of biofilm-infected wounds. *Chem. Eng. J.* **2023**, *459*, 141507.
38. Yan, L.X.; Chen, L.J.; Zhao, X.; et al. pH switchable nanoplatform for *in vivo* persistent luminescence imaging and precise photothermal therapy of bacterial infection. *Adv. Funct. Mater.* **2020**, *30*, 1909042.
39. Bauer, S.; Schmuki, P.; Von Der Mark, K.; et al. Engineering biocompatible implant surfaces: Part I: Materials and surfaces. *Prog. Mater. Sci.* **2013**, *58*, 261–326.
40. Yue, P.; Chen, B.; Lv, X.; et al. Biocompatible composite microspheres of chitin/ordered mesoporous carbon CMK3 for bilirubin adsorption and cell microcarrier culture. *Macromol. Biosci.* **2022**, *22*, 2100412.